A complementary impedance spectroscopy biosensing method with graphene

Biosensors and Bioelectronics 305 (2026) 118679

Contents lists available at ScienceDirect

Biosensors and Bioelectronics

journal homepage: www.elsevier.com/locate/bios

A complementary impedance spectroscopy biosensing method with graphene

Munis Khan [a], Ivan Mijakovic [b,c], Santosh Pandit [b,*], August Yurgens [a,*]

[a] Chalmers University of Technology, Department of Microtechnology and Nanoscience, Gothenburg, SE41296, Sweden
[b] Chalmers University of Technology, Department of Life Sciences, Gothenburg, SE41296, Sweden
[c] Technical University of Denmark, The Novo Nordisk Foundation Center for Biosustainability, Lyngby, 2800, Denmark

ARTICLE INFO

Keywords:
Graphene field-effect transistor
AC impedance
Y/X^2-metric
Baseline stability
Functional-layer capacitance

ABSTRACT

We present a biosensing platform based on a graphene liquid-gate field-effect transistor functionalized with a bioactive layer. The proximity of the graphene channel to the functional layer enables sensitive detection of analyte-induced changes via complex AC impedance of the graphene itself, expressed as $X+iY$. This approach parallels classical Electrochemical Impedance Spectroscopy (EIS), but with current flowing laterally along the graphene channel rather than through the electrolyte between EIS electrodes. We introduce a novel metric, Y/X^2, which at low frequencies is proportional to the effective capacitance arising from three capacitances in series: the quantum capacitance of graphene, the electrical double-layer capacitance, and the capacitance of the functional layer. This metric exhibits high sensitivity to analyte presence and demonstrates excellent baseline stability, making it well-suited for reliable biomarker detection. The technique supports biosensor miniaturization, ensures stable operation, and offers a practical route toward robust and scalable bioelectronic sensing applications.

1. Introduction

Since its discovery, graphene has emerged as one of the most promising two-dimensional (2D) materials for electronics and opto-electronics. This zero-bandgap semiconductor, composed of carbon atoms in a hexagonal lattice (Novoselov et al., 2004), exhibits excellent electrical properties, including high carrier mobility (Tan et al., 2007). These characteristics, combined with its sensitivity to charged species near its vicinity, make graphene an ideal nanomaterial for sensing applications. In particular, graphene field effect transistors (GFET's) have gained significant attention as label-free affinity biosensors due to their ability to translate molecular interactions into electrical signals (Krishnan et al., 2023; Szunerits et al., 2024).

In most GFET biosensors, the gate voltage V_g is applied between the graphene channel and a gate electrode, both immersed in solution, while a constant current I_{ds} flows through the graphene channel. The resulting bell-shaped transfer curve reflects the transition between hole and electron conduction, with the charge-neutrality point (CNP) marking equal carrier populations. The biosensing mechanism is usually attributed to shifts in the CNP, induced by molecular adsorption or molecular binding, resulting in a charge transfer to- or from- graphene. However, detection precision is often hindered by hysteresis due to charge trapping (Wang et al., 2010; Yu et al., 2020; Wei et al., 2020) and time drifts (Miyakawa et al., 2021; Mouro et al., 2025). Additionally, analyte adsorption introduces charge carrier scattering and increases disorder in the system (Chen et al., 2014; Farid et al., 2015).

Electrochemical impedance spectroscopy (EIS) is a valuable method in biosensing, providing detailed information about biorecognition events at the electrode surface. It is used to detect DNA, antigens, antibodies, and bacterial cells (Lazanas and Prodromidis, 2023; Randviir and Banks, 2022). EIS probes the signal response over a wide frequency range (~1 mHz - 1 MHz) and is a non-invasive technique that does not disturb the system's steady state. EIS is highly sensitive to changes on the electrode surface, making it ideal for monitoring surface modifications and can detect very low concentrations of analytes, especially with amplification techniques (Leva-Bueno et al., 2020). However, the results are sensitive to experimental setup and conditions, needing careful control and calibration. Additionally, EIS requires specialized and often expensive equipment (EIS-systems, 2026).

Here, we show that a bio-active functional layer on top of an electrically conducting thin film with sufficiently high sheet resistance can conveniently be used as a complementary EIS biosensing method. The functional-layer properties involving the double-layer capacitance and/or charge-transfer resistance are reflected in the complex impedance of the thin-film in direct contact with the layer. A simple low-frequency setup using a lock-in amplifier is sufficient for

* Corresponding authors.
E-mail addresses: pandit@chalmers.se (S. Pandit), yurgens@chalmers.se (A. Yurgens).

https://doi.org/10.1016/j.bios.2026.118679
Received 2 October 2025; Received in revised form 6 April 2026; Accepted 7 April 2026
Available online 8 April 2026

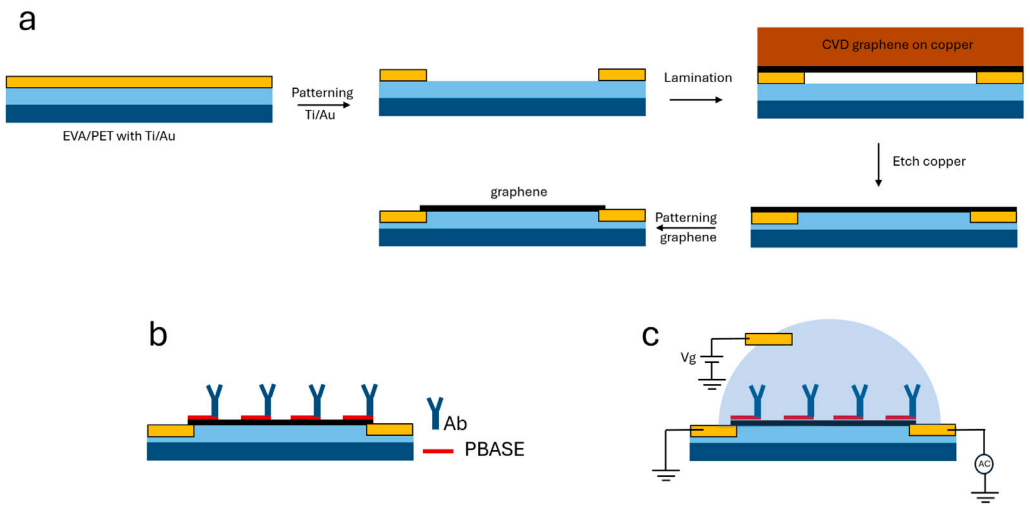

Fig. 1. GFET fabrication. (a) Process flow for graphene transfer from Cu foil to EVA/PET substrate, (b) functionalization and (c) electrical measurement set-up.

such measurements. In the particular case of having graphene as a resistive thin film, the signal can have an additional contribution from the graphene's quantum capacitance, which is also sensitive to charge transfer to- and from graphene. Unlike majority of graphene biosensors, the electrolyte properties, which might change with time due to e.g., dissolution of ambient gases in the liquid, are less important in these measurements. Overall, this approach allows for biosensor miniaturization, its drift-free operation, and a reliable detection of biomarkers with high signal-to-noise ratio.

2. Materials and methods

Here, we present the design and fabrication of an antibody-functionalized GFET biosensor that integrates the high specificity of a bio-receptor (human KLK3/prostate-specific antigen (PSA)) with the highly sensitive detection capabilities of a GFET. This biosensor enables rapid, selective, and label-free detection of the PSA antigen. Fabrication involves multiple stages of conventional microfabrication processing, followed by surface non-covalent functionalization with a molecular linker, which binds to the graphene surface via the π-π stacking interactions (Zhan et al., 2022) (see Fig. 1b). The PSA antibody is immobilized at the graphene channel using carbodiimide cross-linking chemistry (Lepvrier et al., 2014). To minimize non-specific adsorption, the surface of graphene is further blocked with amino-PEG5 alcohol and ethanolamine hydrochloride (Balderston et al., 2021).

2.1. GFET fabrication:

The graphene used in the fabrication of GFET is a monolayer chemical-vapor deposited (CVD) graphene on copper foil. We transfer CVD graphene onto ethylene vinyl acetate (EVA)/polyethylene terephthalate (PET) foil by hot-press lamination with prepatterned electrodes on them (the current-bias-, voltage-, and gate electrodes). Copper foil is etched away chemically by diluted nitric acid (10% HNO_3 in water) followed by graphene patterning using photolithography and oxygen plasma (see Fig. 1a). Overnight annealing at 60 °C under a continuous N_2 flow effectively eliminates volatile residues originating from the wet-etching processes. This treatment does not exhibit any observable degradation of graphene (D'Arsié et al., 2016) and frequently results in high carrier mobilities $\sim 10\,000$ cm^2/(V s) (Khan et al., 2024). Finally, a short piece of plastic tube was attached to the GFET chip by using an epoxy glue to form a small well around graphene channel.

2.2. Functionalization:

Functionalization includes deposition of a single layer of linker molecules of 1-pyrenebutanoic acid succinimidyl ester (PBASE), and a subsequent deposition of biological reagents for target-molecule capture. First, the GFET devices were incubated with PBASE (5 mM in dimethylformamide (DMF) (Sigma-Aldrich)) for 2 h at room temperature and then rinsed in DMF to remove excess PBASE from the surface before blow-drying with N_2. The linker was then conjugated with PSA antibody (Sigma-Aldrich). 30-μL droplets of PSA antibody solution (1 mg/mL) were added to the surface of the chip and left overnight in humid environment at 4 C. The chips were then rinsed in deionized (DI) water and blow-dried. After that, 3 mM PEG5-alcohol (Broadpharm, P-22355) and 1 M ethanolamine hydrochloride (ETA) (Sigma-Aldrich) were used to block the unreacted PBASE molecules. 30-μL droplets of PEG5-alcohol were added to the surface of the chip and left atop for 1 h at room temperature and then rinsed with DI water and blow-dried. The same procedure was repeated for ETA. Fig. 1b shows the functionalized GFET, showing PBASE and antibody attached to the surface of graphene channel.

2.3. Electrical measurements:

Following the incubation and cleaning of GFET sensor chip, the four-probe electrical measurements were performed in a low-ionic strength 0.001 × PBS solution to avoid the charge screening effect, which reduces the observed signal (Shoute et al., 2023). As illustrated in Fig. 1c, an AC bias voltage, $V_b = 250$ mV, with the frequency $f = 137$ Hz, was applied between the current-bias terminals of the GFET through 1 MΩ resistor, to get an almost constant AC current $I_b = 250$ nA. The DC liquid-gate voltage V_g was supplied using Keithley-2604B voltage source meter relative to one of the current-bias electrodes. During the lock-in measurements (SR830, Stanford Research Systems), both the in-phase and the quadrature components of the preamplified (×100) voltage V were recorded to deduce the X and Y components of the sensor-circuit impedance.

For transfer curves $X(V_g)$ and $Y(V_g)$, the GFET's well was filled with 200 μL 0.001 × PBS solution and the chip was allowed to stabilize for five minutes before the gate voltage was swept at a rate of 10 mV/s and both X and Y were recorded before- and after introduction of analyte. The transfer curves were traced while cycling V_g between 0 and −0.3 V three times, eventually resulting in hysteresis-free behavior. For the time-series measurement, the graphene channel was brought to

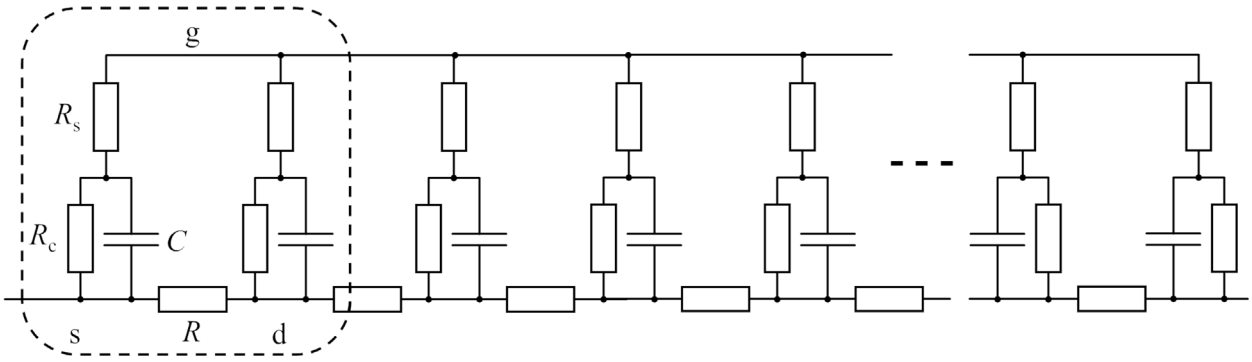

Fig. 2. Lumped-element representation of a distributed Randles circuit. The dashed line delineates a single cell that is examined analytically.

the peak transconductance with the corresponding V_g. Both X and Y components were recorded vs. time before- and after analyte (10 μL droplets of varying concentration) was added to the sensor well.

With multiple tests on one and the same device, the sensor's responsivity declines as the antibodies become saturated and are no longer available to bind additional antigens. All analytes were prepared in the same 0.001 × PBS buffer, to avoid, no matter how small, changes of pH-value of the solution in the well upon adding analyte. DC measurements were done by using the Keithley-2604B voltage source or just a battery and measuring the preamplified DC voltage V_{ds} by the HP-34401 multimeter.

2.4. Model:

The GFET with a liquid gate can be modeled by a network of resistive and capacitive components, as shown in Fig. 2, representing a lumped-element approximation of the distributed Randles equivalent circuit. For simplicity, we analyze just one element of such a circuit. Here R_s is the solution resistance, R_c is the charge transfer resistance of the double layer, R is the in-plane resistance of graphene, and ω is the angular frequency. Graphene has a wide electrochemical window in electrolytic environment resulting in a very high $R_c \gg R, R_s$ (Silva et al., 2025), which can hence be neglected. Since we used a highly diluted buffer (0.001 × PBS), R_s can also be large, $R_s \geq R$.

The graphene–electrolyte interface can be modeled as a series combination of three capacitances in series. The first capacitance is the double-layer capacitance C_{dl}, which appears at the interface between a charged electrode and a fluid. Next is the capacitance of the bio-functional layer C_f, consisting of antibodies and surface-blocking molecules. Finally, the quantum capacitance C_q that accounts for the variation of the density of states with Fermi level must also be considered for graphene electrodes.

We anticipate that $C_{dl} \gtrsim C_q > C_f$ and therefore $C = (C_{dl}^{-1} + C_q^{-1} + C_f^{-1})^{-1} \sim C_f$ (see parameter estimations in Sec. S1b of the Supplementary Information (SI)). The X and Y components of the circuit impedance are given by the following equations:

$$X = \frac{2R\left[\omega^2 C^2 R_s(R+2R_s)+2\right]}{\omega^2 C^2 (R+2R_s)^2+4} \rightarrow R \text{ for } \omega C(R+2R_s) \ll 2 \quad (1)$$

$$Y = -\frac{2\omega C R^2}{\omega^2 C^2 \left(R+2R_s\right)^2+4} \rightarrow -\frac{\omega C R^2}{2} \text{ for } \omega C(R+2R_s) \ll 2 \quad (2)$$

From these simple equations we have discovered an intriguing metric that enables direct access to the effective capacitance of the adjacent layers on top of graphene. Specifically, this metric is represented by the ratio Y/X^2 and for low enough ω:

$$\frac{Y}{X^2} = -\frac{\omega C\left[\omega^2 C^2 (R+2R_s)^2+4\right]}{2\left[\omega^2 C^2 R_s(R+2R_s)+2\right]^2} \rightarrow -\frac{\omega C}{2} \text{for } \omega C(R+2R_s) \ll 2. \quad (3)$$

The convenience of this metric lies in its low-frequency operation, which allows for the use of inexpensive electronics in practical biosensor devices. In practice, the condition $\omega C(R+2R_s) \ll 2$ is normally fulfilled for frequencies below some 300–500 Hz and diluted buffer, 0.01 × PBS or 0.001 × PBS (see SI for a more detailed discussion). In the case of graphene, this metric is also not affected by baseline drifts with time t, $R(t)$, common in DC measurements. These drifts are likely caused by changes in graphene doping due to external factors, such as variations in the solution temperature and its pH value, which may result from the dissolution of CO_2 in water. Even pH of buffer solutions is not constant and depends on ionic strength and temperature (Wikipedia contributors, 2025).

3. Results and discussion

Real-time biosensing using GFET's typically involves monitoring conductance or resistance over time at a fixed V_g. The optimal response occurs in the high transconductance regions (Saltzgaber et al., 2013), but this also amplifies a low-frequency noise, which degrades sensitivity (Fu et al., 2017; Mavredakis et al., 2018). Furthermore, the baseline drift remains a major challenge in GFET's even in the absence of target molecules (Ushiba et al., 2020; Miyakawa et al., 2021; Ushiba et al., 2024). Practical sensor designs must also account for interfacial capacitance changes upon bio-molecular adsorption (Kim and Kim, 2026).

Unlike methods that focus largely on DC conductance, we use AC bias and a low-frequency lock-in amplifier to extract information about dynamic charge transport and electrostatic interactions. We demonstrate that using AC bias enhances biosensor sensitivity and accuracy by simultaneously capturing both resistance and capacitance changes during bio-molecular interactions. Our method provides direct access to the effective capacitance C resulting from the three capacitances in series, C_q (Wang et al., 2016; C. Wang et al., 2016; Pourasl et al., 2019), C_{dl} (Chen et al., 2012; Munje et al., 2015), and C_f.

Because of relatively low charge-carrier density in graphene, the quantum capacitance can become important in biosensing (Ebrish et al., 2014; Deen et al., 2013; Ebrish et al., 2012; Hassan et al., 2023). Analyte adsorption alters graphene's carrier density, leading to measurable shifts in Fermi energy and quantum capacitance (C. Wang et al., 2016; Pourasl et al., 2019; Zhang et al., 2017; Xia et al., 2009; Chen et al., 2010; Mackin et al., 2014).

The functional molecules on top of graphene create an ion-permeable charged layer involving accumulation of counter-ions required to maintain the charge neutrality. The concentration difference between the buffer solution and the immobilized ion-permeable layer establishes the Donnan potential (Ohshima and Ohki, 1985; Bergveld, 1991), which further modifies the electric field between graphene and gate electrode. This additional potential alters the graphene-channel resistance (R_{ch}), thereby extending sensing beyond the Debye screening length (Palazzo et al., 2014; Gao et al., 2015).

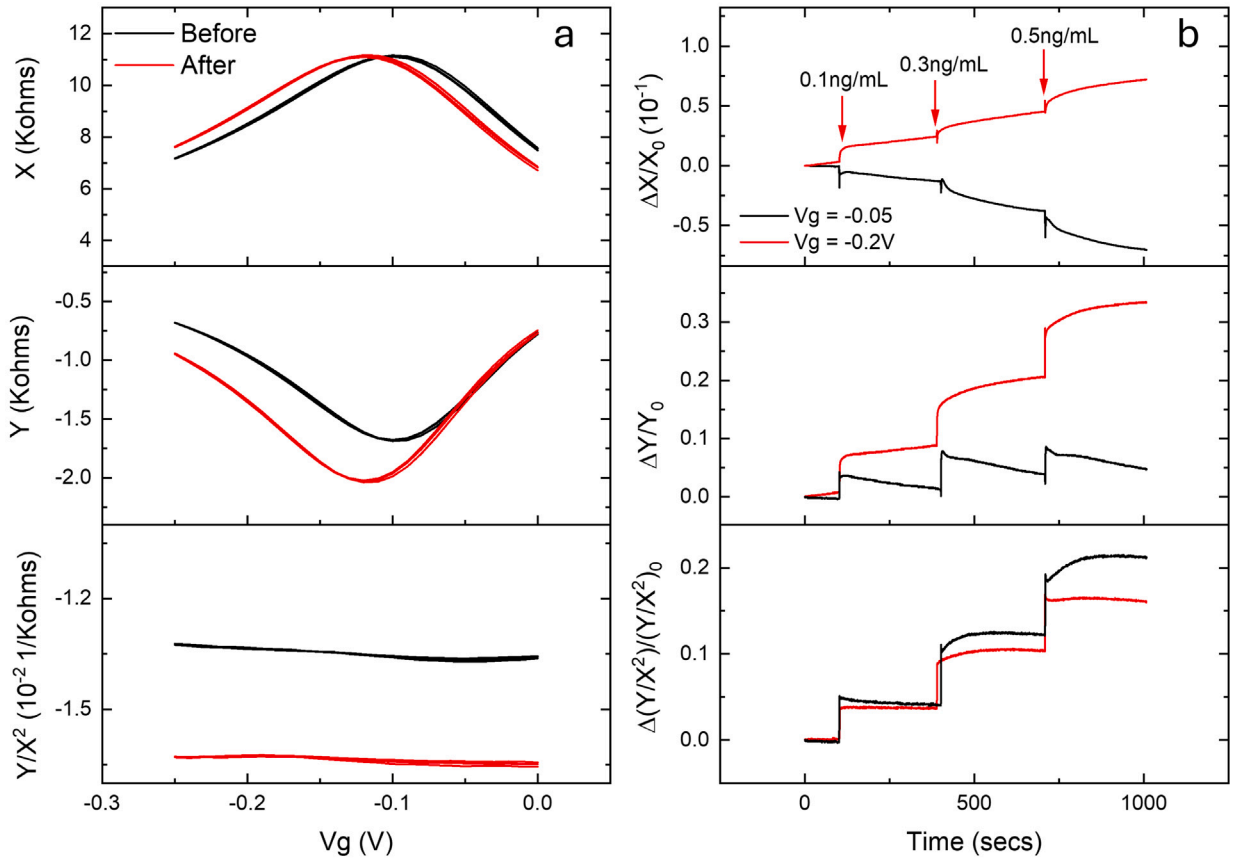

Fig. 3. Gate dependence and analyte detection. (a) Transfer curves and corresponding (b) time series measurements at V_g −0.05 V and −0.2 V of an PSA antibody functionalized GFET exposed to target analyte. Before and after transfer curves in (a) correspond to time points 0 s and 1000 s, respectively, in (b). The red arrows indicate the moments when the analyte concentration in the well changed to the specified values.

3.1. Lock-in measurements

The measurements of X and Y versus V_g were performed before and after analyte introduction, as shown in Fig. 3a. A shift in X suggests changes in R_{ch}, likely due to charge transfer (Béraud et al., 2021) initiated by analyte binding. A shift in Y includes changes of effective capacitance C. It has been assumed that it is driven by variations in quantum capacitance (Deen et al., 2013; Zhang et al., 2017; Hassan et al., 2023) and/or modifications in the electric double layer (Munje et al., 2015; Chen et al., 2012; Randviir and Banks, 2022). These changes occur through multiple mechanisms, including ion redistribution in the EDL, which alters its capacitance C_{dl}, charge transfer, which modifies C_q (Deen et al., 2013; Zhang et al., 2017; Hassan et al., 2023), and changes in the local dielectric constant (k), as the analyte displaces water molecules or introduces molecular dipoles, affecting C_f (Thriveni and Ghosh, 2022). It seems that C_f is the smallest of the three capacitances and is therefore the main sensing readout element in our devices (see SI for capacitance comparison).

As illustrated in Fig. 3a, the variations in Y were more pronounced than those in X, indicating a substantial capacitive component in the sensing response. To further investigate this, we used our new metric, $Y/X^2(V_g)$, and analyzed its behavior before- and after adding analyte. This metric effectively decouples capacitive effects from resistive contributions (see Eq. (3)). Notably, Y/X^2 remains nearly constant across the entire V_g range, in contrast to the strongly non-linear behavior of both $X(V_g)$ and $Y(V_g)$ (see Fig. 3a). This highlights the utility of Y/X^2 in isolating capacitive changes associated with biomolecular binding. Compared to the conventional approach of monitoring changes in graphene resistance, this parameter offers more stable operation and improved reliability in analyte detection.

To validate this metric further, we performed time-series measurements (Fig. 3b) by fixing V_g at the peak transconductance points and continuously monitoring X, Y, and Y/X^2 as the analyte was introduced. The GFET was exposed to different analyte concentrations at some time intervals, indicated by the red vertical arrows in Fig. 3b. The electrical response was normalized to the values at $t = 0$, i.e., $\Delta X/X_0 = (X - X_0)/X_0$, where $X_0 = X(t = 0)$, etc. A significant drift in X is seen, which obscures the response to adding the analyte. On the contrary, Y/X^2 provided a much more stable baseline and, therefore, a clearer response. It also demonstrated a higher signal-to-noise ratio (SNR) and minimal dependency on V_g, ensuring consistent results across different operating points.

To check how specific is the response of the functionalized GFET to the target analyte, we conducted several control tests with a non-target protein, bovine serum albumin (BSA) (see Fig. 4a). The red arrows in Fig. 4a indicate the time intervals when either the target protein (PSA) or the non-target protein (BSA) was introduced onto the GFET (see Methods). As evident in Fig. 4a, the GFET functionalized for PSA exhibits a distinct response only to the target analyte (PSA), confirming its specificity (see Sec. S8 where we demonstrate specificity against another non-target protein, DefA).

To further validate our results, we tested a non-functionalized GFET (without PSA antibodies) by exposing it to varying concentrations of PSA antigen. The results were then compared with those from the functionalized GFET (with PSA antibodies), as shown in Fig. 4a. While a small shift in response was observed for the non-functionalized GFET, the response of the functionalized GFET to PSA at the same concentrations was significantly larger. The minor response in the non-functionalized GFET is likely due to non-specific bindings of PSA to the graphene surface.

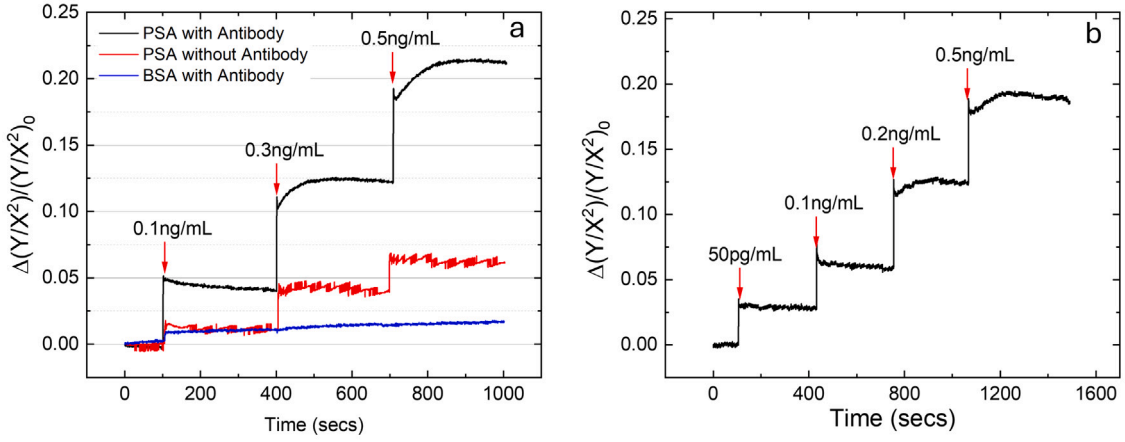

Fig. 4. Detection selectivity and sensitivity. (a) Selective response of a PSA antibody functionalized GFET towards target analyte PSA (black line) and non-target analyte BSA (blue line), also shown is a response of a non-functionalized (without PSA antibody) to target analyte PSA (red line). (b) Real time response of a PSA antibody functionalized GFET towards varying concentrations of target analyte PSA, inset shows a SNR to the 50 pg/mL concentration. The red arrows indicate the moments when the analyte concentration in the well changed to the specified values.

To evaluate the sensitivity of the GFET biosensor, we conducted real-time measurements by introducing lower concentrations of the target analyte (Fig. 4b). The experiment started by adding 10 μL of a stock PSA solution to 200 μL of buffer in the GFET well, yielding an analyte concentration of 50 pg/mL. This concentration corresponds to 1.6 pM, assuming the molecular weight of PSA antigen of ~ 30 000 Da. A significant response was observed with a high signal-to-noise ratio (see the inset of Fig. 4b), demonstrating the sensor's ability to detect PSA at extremely low concentrations. For prostate cancer, a PSA level greater than 4.0 ng/mL is typically regarded as abnormal, potentially leading to a recommendation for a prostate biopsy. However, since PSA levels naturally rise with age, some doctors use a higher threshold (e.g., 5 ng/mL) for older men and a lower threshold (e.g., 2.5 ng/mL) for younger men (Gulati et al., 2013). Here, a much lower concentration of 50 pg/mL was reliably detected by our sensor demonstrating its high sensitivity.

3.2. Frequency-dependent impedance response

In a typical biosensing EIS, the experiment is run over a wide range of frequencies to observe changes in R_c and C_{dl}. At high frequencies, the impedance response is dominated by C_{dl}, which decreases upon antigen binding due to reduced ion mobility and changes in dielectric properties. At low frequencies, the impedance is controlled by R_c, which increases as the antigen layer blocks electron transfer (Lazanas and Prodromidis, 2023; Randviir and Banks, 2022).

Previous EIS studies have used the Constant Phase Element (CPE) model to explain deviations from purely capacitive behavior of the electrolyte–graphene interface, which could potentially account for our observations as well. For instance, the electrolyte–graphene interface was found to exhibit CPE behavior, with both the admittance parameter Q_0 and phase factor α varying with frequency (Sun and Liu, 2019). The study suggested that charged impurities and defects in the graphene lattice introduce inhomogeneous charge distribution, leading to frequency-dependent capacitance.

Similarly, in Garcia-Cortadella et al. (2020), a detailed characterization of liquid-gate GFET's frequency response revealed that signal distortion and transconductance reduction at higher frequencies arise due to deviations from the ideal-capacitor behavior. The study found that at low frequencies, ions in the electrolyte fully contribute to double-layer charging, enhancing the capacitance and gate modulation efficiency. However, at higher frequencies, ionic-mobility constraints and capacitive leakage currents suppress the effective gate capacitance, causing weaker electrostatic control of the graphene channel.

There is a substantial increase in the Y/X^2 response at higher frequencies for the same analyte concentration (see also Sec. S11 and Fig. S15). This can be attributed to the fact that Y/X^2 reflects interfacial capacitance changes, which are more dominant at high frequencies. To further explore these effects, we conducted time-series measurements at different frequencies. We tracked the evolution of X, Y, and Y/X^2 over time for different frequencies at a constant V_g corresponding to the peak transconductance while introducing the analyte in steps of increasing concentration (see Fig. 5a). The shift in Y/X^2 increased with frequency for the same analyte concentration.

Interestingly, we also observed a reversal of the shift direction in X at higher frequencies while the shift in Y first increases and then decreases from 375 Hz and onward. The observed behavior is likely due to the non-ideal nature of the electrolyte–graphene interface, where variations in interfacial capacitance cause the $X(V_g)$ curve to shift downward at higher frequencies. However, a complete explanation of all experimental details remains challenging. Notably, the distinct shift in the charge neutrality point of $X(V_g) \approx R(V_g)$ at the lowest frequency upon analyte addition suggests charge transfer to graphene. Simultaneously, changes in $Y/X^2 \approx \omega C/2$ indicate modifications in capacitance. As frequency increases, the condition $\omega C(R + 2R_s) \ll 2$ eventually breaks down, and the full expressions—rather than the simplified forms in Eqs. (1) and (2)—must be considered. The derived metric Y/X^2, which has proved to be useful for isolating changes in C, becomes then dependent on R at high frequencies, diminishing its utility (see Eq. (3)). Even for constant R, the response in Y/X^2 can vanish at a specific frequency, determined by solving $\partial(Y/X^2)/\partial C = 0$ (see Eqs. S5 and S6 in SI). Looking ahead, one promising direction could be to replace graphene with a highly resistive thin film. This would eliminate the influence of charge transfer and allow the system to fully exploit this EIS analog, focusing purely on capacitive changes at the interface (see Sec. S7 of SI).

Our GFET biosensor remains to be highly selective also at 1000 Hz, which was concluded from comparison of sensor responses to the target- (PSA) and a non-target control (BSA) analytes (see Fig. 5b, and also Fig. 5a showing the results at 137 Hz). The sensor exhibited excellent selectivity, demonstrating a strong response to PSA, while the response to BSA was almost negligible. This confirms that the measured changes in both the resistive (X) and capacitive (Y) components, as well as in the derived Y/X^2 ratio, are primarily due to the specific binding of the target analyte rather than non-specific interactions. The minimal response to BSA (non-target analyte) confirms the sensor's detection specificity.

Finally, we compared the Y/X^2 response at 1000 Hz to a conventional DC measurement of graphene resistance (see Fig. 5c). Both

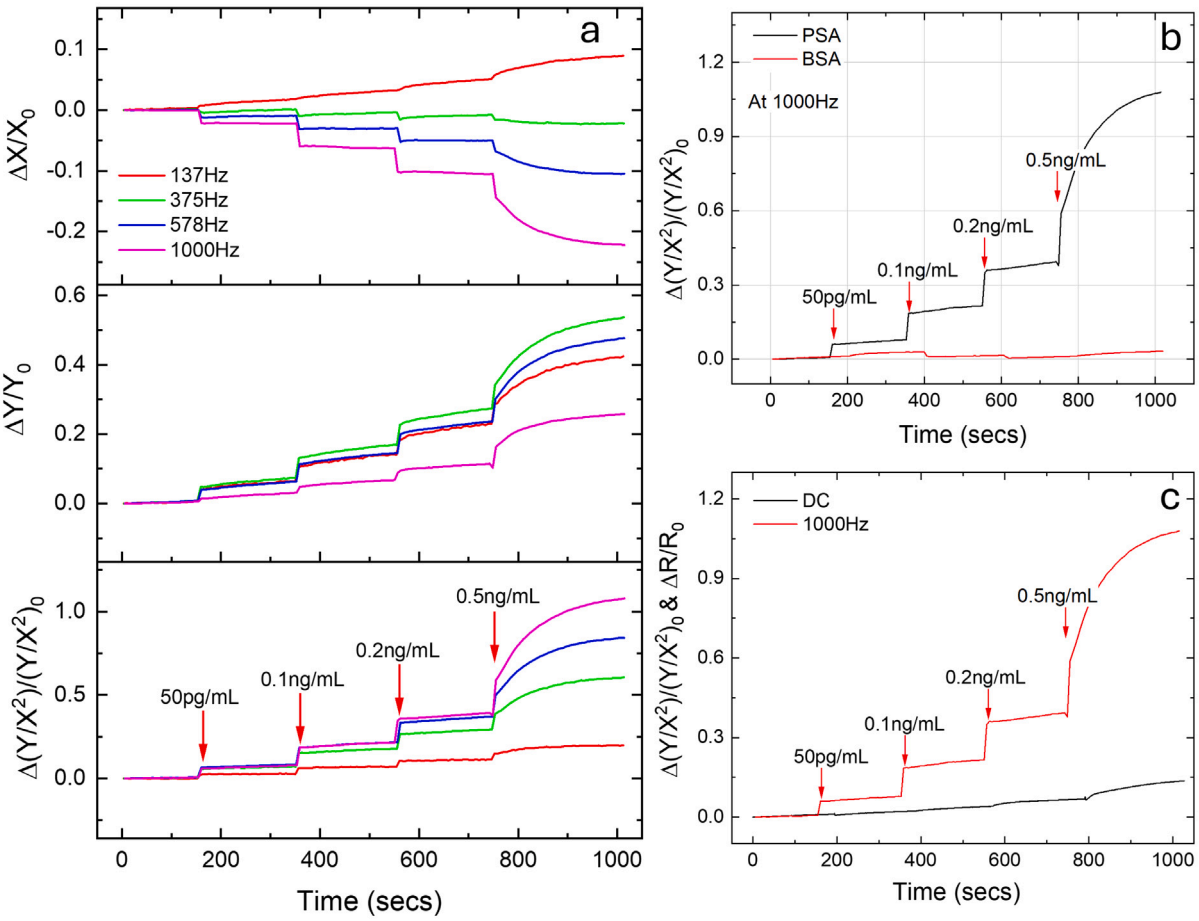

Fig. 5. Frequency dependence of time-series response. (a) Time-series response of a PSA antibody functionalized GFET towards varying concentrations to target analyte PSA at different frequencies ($V_g = 0.2V$). (b) Normalized Y/X^2 response to target (PSA) and non-target (BSA) at 1000 Hz. (c) Normalized DC resistance ($\Delta R/R_0$) vs. normalized Y/X^2 response to target (PSA) analyte ($V_g = 0.2V$). The red arrows indicate the moments when the analyte concentration in the well changed to the specified values.

DC and AC measurements were performed on the same device using the same analyte, ensuring a direct comparison between the two approaches. The results clearly demonstrate that the lock-in measurement response far exceeds what can be detected using conventional DC methods. The significantly higher sensitivity observed in the lock-in measurement highlights the advantage of frequency-based detection, where enhanced capacitive contributions and improved noise rejection enable the detection of subtle bio-molecular interactions that remain undetectable in conventional resistance-based sensing. This confirms that Y/X^2 at higher frequencies provides a superior biosensing strategy, offering enhanced sensitivity and robustness over traditional methods.

4. Conclusion

In conclusion, we have introduced a complementary Electrochemical Impedance Spectroscopy (EIS) method for biosensing. In this approach, the AC bias current is applied through graphene that is in direct contact with the bio-functional layer, rather than through the electrolyte as in traditional EIS. The bio-functional layer can be engineered to undergo well-defined changes upon specific molecular bindings, and the in-phase (X) and quadrature (Y) components of the sensor impedance provide rich information about these changes. A new and useful metric, Y/X^2, has been identified, which effectively isolates variations in the capacitance of both the bio-functional layer and the adjacent electrolyte double layer.

Using graphene liquid-gate transistor biosensors, specific antibody–antigen binding was reliably detected even at low analyte concentrations. The sensor response remained free from noise and the baseline drift often observed in graphene biosensors that rely on conventional DC resistance measurements. It should be emphasized, however, that the present validation was carried out under low ionic-strength conditions, where the Debye length is sufficiently large to enable efficient signal transduction. As such, the performance demonstrated here cannot yet be generalized to physiological or otherwise high-ionic-strength environments. Future work will explicitly target extending this method to higher ionic-strength media to evaluate robustness, signal transduction pathways, and practical applicability under more realistic conditions.

Most importantly, this method is not limited to graphene biosensors. It can be broadly applied to any conducting thin films with sufficiently high sheet resistance. This versatility expands the range of potential biosensing platforms by enabling the tailored design of chemical linkers between the resistive-film material and antibodies or other functional molecules.

CRediT authorship contribution statement

Munis Khan: Writing – review & editing, Writing – original draft, Methodology, Investigation, Formal analysis, Conceptualization. **Ivan Mijakovic:** Writing – review & editing, Supervision, Funding acquisition. **Santosh Pandit:** Writing – review & editing, Validation, Supervision, Investigation. **August Yurgens:** Writing – review & editing,

Supervision, Resources, Investigation, Funding acquisition, Conceptualization.

Declaration of competing interest

M.K., S.P., and A.Y. are co-owners of LayerLogic AB, a company that develops devices and methods similar to those described in this manuscript. A patent application titled "Complementary electrochemical impedance spectroscopy method in sensor devices" has been filed by A.Y. and M.K. with the Swedish Patent and Registration Office (PRV), application number 2530180-5 (2025). The authors declare no other competing interests.

Acknowledgments

This research has received funding from the European Union's Horizon 2020 research and innovation programme under the Marie Skłodowska-Curie grant agreement No 955626 and Nordic Programme for Interdisciplinary Research, grant 105121. Support from 2D-TECH (Vinnova) competence center is highly appreciated. SP acknowledges funding from Vetenskapsrådet (2020–04096) and Vinnova 2023-04134. IM acknowledges funding from Novo Nordisk Foundation [NNF20CC0035580]. This work was performed in part at Myfab Chalmers.

Appendix A. Supplementary data

Supplementary data to this article can be found online at https://doi.org/10.1016/j.bios.2026.118679.

Data availability

Data sets generated during the current study are available from the corresponding author on reasonable request.

References

Balderston, S., Taulbee, J.J., Celaya, E., Fung, K., Jiao, A., Smith, K., Hajian, R., Gasiunas, G., Kutanovas, S., Kim, D., et al., 2021. Discrimination of single-point mutations in unamplified genomic DNA via Cas9 immobilized on a graphene field-effect transistor. Nat. Biomed. Eng. 5 (7), 713–725.

Béraud, A., Sauvage, M., Bazán, C.M., Tie, M., Bencherif, A., Bouilly, D., 2021. Graphene field-effect transistors as bioanalytical sensors: Design, operation and performance. Analyst 146 (2), 403–428.

Bergveld, P., 1991. A critical evaluation of direct electrical protein detection methods. Biosens. Bioelectron. 6 (1), 55–72.

Chen, Y., Michael, Z.P., Kotchey, G.P., Zhao, Y., Star, A., 2014. Electronic detection of bacteria using holey reduced graphene oxide. ACS Appl. Mater. Interfaces 6 (6), 3805–3810.

Chen, F., Qing, Q., Xia, J., Tao, N., 2010. Graphene field-effect transistors: Electrochemical gating, interfacial capacitance, and biosensing applications. Chemistry–an Asian J. 5 (10), 2144–2153.

Chen, S., Zhang, Z.B., Ma, L., Ahlberg, P., Gao, X., Qiu, Z., Wu, D., Ren, W., Cheng, H.M., Zhang, S.L., 2012. A graphene field-effect capacitor sensor in electrolyte. Appl. Phys. Lett. 101 (15).

D'Arsié, L., Esconjauregui, S., Weatherup, R.S., Wu, X., Arter, W.E., Sugime, H., Cepek, C., Robertson, J., 2016. Stable, efficient p-type doping of graphene by nitric acid. RSC Adv. 6, 113185–113192. http://dx.doi.org/10.1039/C6RA23727D.

Deen, D.A., Olson, E.J., Ebrish, M.A., Koester, S.J., 2013. Graphene-based quantum capacitance wireless vapor sensors. IEEE Sensors J. 14 (5), 1459–1466.

Ebrish, M.A., Olson, E.J., Koester, S.J., 2014. Effect of noncovalent basal plane functionalization on the quantum capacitance in graphene. ACS Appl. Mater. Interfaces 6 (13), 10296–10303.

Ebrish, M., Shao, H., Koester, S., 2012. Operation of multi-finger graphene quantum capacitance varactors using planarized local bottom gate electrodes. Appl. Phys. Lett. 100 (14).

EIS-systems, 2026. See e.g., https://www.biologic.net/products/vsp-300/, https://www.el-cell.com/products/, and https://www.palmsens.com/product-select/ for more information.

Farid, S., Meshik, X., Choi, M., Mukherjee, S., Lan, Y., Parikh, D., Poduri, S., Baterdene, U., Huang, C.-E., Wang, Y.Y., et al., 2015. Detection of interferon gamma using graphene and aptamer based FET-like electrochemical biosensor. Biosens. Bioelectron. 71, 294–299.

Fu, W., Feng, L., Panaitov, G., Kireev, D., Mayer, D., Offenhäusser, A., Krause, H.J., 2017. Biosensing near the neutrality point of graphene. Sci. Adv. 3 (10), e1701247.

Gao, N., Zhou, W., Jiang, X., Hong, G., Fu, T.M., Lieber, C.M., 2015. General strategy for biodetection in high ionic strength solutions using transistor-based nanoelectronic sensors. Nano Lett. 15 (3), 2143–2148.

Garcia-Cortadella, R., Masvidal-Codina, E., De la Cruz, J.M., Schäfer, N., Schwesig, G., Jeschke, C., Martinez-Aguilar, J., Sanchez-Vives, M.V., Villa, R., Illa, X., et al., 2020. Distortion-free sensing of neural activity using graphene transistors. Small 16 (16), 1906640.

Gulati, R., Gore, J.L., Etzioni, R., 2013. Comparative effectiveness of alternative prostate-specific antigen–based prostate cancer screening strategies: model estimates of potential benefits and harms. Ann. Intern. Med. 158 (3), 145–153.

Hassan, A., Mattioli, I.A., Colombo, R.N., Crespilho, F.N., 2023. Tuning quantum capacitance in 2D graphene electrodes: the role of defects and charge carrier concentration. J. Mater. Chem. C 11 (19), 6301–6305.

Khan, M., Ji, J., Zhou, B., Jepsen, P.U., Bøggild, P., Yurgens, A., 2024. High mobility graphene field effect transistors on flexible EVA/PET foils. In: 2D Materials. 11 (3), 035022.

Kim, N.-S., Kim, J., 2026. Advancing non-faradaic impedance biosensors: sensitivity enhancement strategies using microfluidics, multiscale labeling, and CMOS technology. Microsystems Nanoeng. 12 (1), 117.

Krishnan, S.K., Nataraj, N., Meyyappan, M., Pal, U., 2023. Graphene-based field-effect transistors in biosensing and neural interfacing applications: recent advances and prospects. Anal. Chem. 95 (5), 2590–2622.

Lazanas, A.C., Prodromidis, M.I., 2023. Electrochemical impedance spectroscopy a tutorial. ACS Meas. Sci. Au 3 (3), 162–193.

Lepvrier, E., Doigneaux, C., Moullintraffort, L., Nazabal, A., Garnier, C., 2014. Optimized protocol for protein macrocomplexes stabilization using the EDC, 1-ethyl-3-(3-(dimethylamino) propyl) carbodiimide, zero-length cross-linker. Anal. Chem. 86 (21), 10524–10530.

Leva-Bueno, J., Peyman, S.A., Millner, P., 2020. A review on impedimetric immunosensors for pathogen and biomarker detection. Med. Microbiol. Immunol. 209 (3), 343–362.

Mackin, C., Hess, L.H., Hsu, A., Song, Y., Kong, J., Garrido, J.A., Palacios, T., 2014. A current–voltage model for graphene electrolyte-gated field-effect transistors. IEEE Trans. Electron Devices 61 (12), 3971–3977.

Mavredakis, N., Cortadella, R.G., Calia, A.B., Garrido, J.A., Jiménez, D., 2018. Understanding the bias dependence of low frequency noise in single layer graphene FETs. Nanoscale 10 (31), 14947–14956.

Miyakawa, N., Shinagawa, A., Kajiwara, Y., Ushiba, S., Ono, T., Kanai, Y., Tani, S., Kimura, M., Matsumoto, K., 2021. Drift suppression of solution-gated graphene field-effect transistors by cation doping for sensing platforms. Sensors 21 (22), 7455.

Mouro, J., Domingues, T., Pereira, T., Campos, R., Borme, J., Alpuim, P., 2025. Analytical modeling and experimental characterization of drift in electrolyte-gated graphene field-effect transistors. Npj 2D Mater. Appl. 9 (1), 26.

Munje, R.D., Muthukumar, S., Panneer Selvam, A., Prasad, S., 2015. Flexible nanoporous tunable electrical double layer biosensors for sweat diagnostics. Sci. Rep. 5 (1), 14586.

Novoselov, K.S., Geim, A.K., Morozov, S.V., Jiang, D.e., Zhang, Y., Dubonos, S.V., Grigorieva, I.V., Firsov, A.A., 2004. Electric field effect in atomically thin carbon films. Science 306 (5696), 666–669.

Ohshima, H., Ohki, S., 1985. Donnan potential and surface potential of a charged membrane. Biophys. J. 47 (5), 673–678.

Palazzo, G., De Tullio, D., Magliulo, M., Mallardi, A., Intranuovo, F., Mulla, M.Y., Favia, P., Vikholm-Lundin, I., Torsi, L., 2014. Detection beyond Debye's length with an electrolyte-gated organic field-effect transistor. Adv. Mater. (Deerfield Beach, Fla.) 27 (5), 911–916.

Pourasl, A.H., Ariffin, S.H.S., Ahmadi, M., Gharaei, N., Rashid, R.A., Ismail, R., 2019. Quantum capacitance model for graphene FET-based gas sensor. IEEE Sensors J. 19 (10), 3726–3732.

Randviir, E.P., Banks, C.E., 2022. A review of electrochemical impedance spectroscopy for bioanalytical sensors. Anal. Methods 14 (45), 4602–4624.

Saltzgaber, G., Wojcik, P.M., Sharf, T., Leyden, M.R., Wardini, J.L., Heist, C.A., Adenuga, A.A., Remcho, V.T., Minot, E.D., 2013. Scalable graphene field-effect sensors for specific protein detection. Nanotechnology 24 (35), 355502.

Shoute, L.C., Abdelrasoul, G.N., Ma, Y., Duarte, P.A., Edwards, C., Zhuo, R., Zeng, J., Feng, Y., Charlton, C.L., Kanji, J.N., et al., 2023. Label-free impedimetric immunosensor for point-of-care detection of COVID-19 antibodies. Microsystems Nanoeng. 9 (1), 3.

Silva, L.d.S., Oliveira, L.B., Fonseca, T.L., Colherinhas, G., 2025. Structural and electrochemical properties of graphene-based supercapacitors with water and methanol-co-solvated ionic liquids: a molecular dynamics study. J. Mol. Liq. 434, 128041.

Sun, J., Liu, Y., 2019. Unique constant phase element behavior of the electrolyte–graphene interface. Nanomaterials 9 (7), 923.

Szunerits, S., Rodrigues, T., Bagale, R., Happy, H., Boukherroub, R., Knoll, W., 2024. Graphene-based field-effect transistors for biosensing: where is the field heading to? Anal. Bioanal. Chem. 416 (9), 2137–2150.

Tan, Y.-W., Zhang, Y., Bolotin, K., Zhao, Y., Adam, S., Hwang, E., Das Sarma, S., Stormer, H., Kim, P., 2007. Measurement of scattering rate and minimum conductivity in graphene. Phys. Rev. Lett. 99 (24), 246803.

Thriveni, G., Ghosh, K., 2022. Advancement and challenges of biosensing using field effect transistors. Biosensors 12 (8), 647.

Ushiba, S., Okino, T., Miyakawa, N., Ono, T., Shinagawa, A., Kanai, Y., Inoue, K., Takahashi, K., Kimura, M., Matsumoto, K., 2020. State-space modeling for dynamic response of graphene FET biosensors. Japan. J. Appl. Phys. 59 (SG), SGGH04.

Ushiba, S., Tokuda, Y., Nakano, T., Ono, T., Tani, S., Kimura, M., Matsumoto, K., 2024. Drift suppression of solution-gated graphene field-effect transistors through electrolyte submersion. Appl. Phys. Express 17 (4), 045002.

Wang, C., Li, Y., Zhu, Y., Zhou, X., Lin, Q., He, M., 2016. High-κ solid-gate transistor configured graphene biosensor with fully integrated structure and enhanced sensitivity. Adv. Funct. Mater. 26 (42), 7668–7678.

Wang, L., Wang, W., Xu, G., Ji, Z., Lu, N., Li, L., Liu, M., 2016. Analytical carrier density and quantum capacitance for graphene. Appl. Phys. Lett. 108 (1).

Wang, H., Wu, Y., Cong, C., Shang, J., Yu, T., 2010. Hysteresis of electronic transport in graphene transistors. ACS Nano 4 (12), 7221–7228.

Wei, J., Liang, B., Cao, Q., Ren, H., Zheng, Y., Ye, X., 2020. Understanding asymmetric transfer characteristics and hysteresis behaviors in graphene devices under different chemical atmospheres. Carbon 156, 67–76.

Wikipedia contributors, 2025. Phosphate-buffered saline — Wikipedia, the free encyclopedia. Online; URL: https://en.wikipedia.org. (Accessed 1 March 2025).

Xia, J., Chen, F., Li, J., Tao, N., 2009. Measurement of the quantum capacitance of graphene. Nature Nanotechnology 4 (8), 505–509.

Yu, T., Kravets, V.G., Imaizumi, S., Grigorenko, A.N., 2020. Effect of dielectric fabrication techniques on graphene gating. J. Phys. Chem. C 125 (1), 865–872.

Zhan, J., Lei, Z., Zhang, Y., 2022. Non-covalent interactions of graphene surface: Mechanisms and applications. Chem 8 (4), 947–979.

Zhang, Y., Ma, R., Zhen, X.V., Kudva, Y.C., Bühlmann, P., Koester, S.J., 2017. Capacitive sensing of glucose in electrolytes using graphene quantum capacitance varactors. ACS Appl. Mater. Interfaces 9 (44), 38863–38869.